

Record spintronic harvesting of thermal fluctuations using paramagnetic molecular centers

B. Chowrira^{1,2*}, L. Kandpal^{1*}, D. Mertz¹, C. Kieber¹, A. Bahouka⁴, R. Bernard¹, L. Joly¹, E. Monteblanco³, S. Mohapatra¹, E. Sternitzky¹, V. Da Costa¹, M. Hehn³, F. Montaigne³, B. Vilen⁵, F. Choueikani², P. Ohresser², D. Lacour³, W. Weber¹, S. Boukari¹, M. Bowen^{1@}

¹Institut de Physique et Chimie des Matériaux de Strasbourg, UMR 7504 CNRS, Université de Strasbourg, 23 Rue du Laëss, BP 43, 67034 Strasbourg, France.

²Synchrotron SOLEIL, L'Orme des Merisiers, Saint-Aubin, BP 48, 91192 Gif-sur-Yvette, France

³Institut Jean Lamour UMR 7198 CNRS, Université de Lorraine, BP 70239, 54506 Vandœuvre les Nancy, France.

⁴IREPA LASER, Institut Carnot MICA, Parc d'innovation - Pole API, 67400 Illkirch, France

⁵Institut de Chimie, UMR 7177 CNRS, Université de Strasbourg, 4 Rue Blaise Pascal, CS 90032, 67081 Strasbourg, France.

*: these authors contributed equally.

@: bowen@unistra.fr

Abstract (208 words)

Experiments and theory are reexamining how the laws of thermodynamics are expressed in a quantum world. Most quantum thermodynamics research is performed at sub-Kelvin temperatures to prevent thermal fluctuations from smearing the quantum engine's discrete energy levels that mediate the asymmetric shuffling of electrons between the electrodes. Meanwhile, several groups report that building an electron-spin based implementation by placing the discrete spin states of paramagnetic centers between ferromagnetic electrodes can not only overcome this drawback, but also induce a net electrical power output despite an apparent thermal equilibrium. We illustrate this thermodynamics conundrum through measurements on several devices of large output power, which endures beyond room temperature. We've inserted the Co paramagnetic center in Co phthalocyanine molecules between electron spin-selecting Fe/C₆₀ interfaces within vertical molecular nanojunctions. We observe output power as high as 450nW(24nW) at 40K(360K), which leapfrogs previous results, as well as classical spintronic energy harvesting strategies involving a thermal gradient. Our data links magnetic correlations between the fluctuating paramagnetic centers and output power. This device class also behaves as a spintronically controlled switch of current flow, and of its direction. We discuss the conceptual challenges raised by these measurements. Better understanding the phenomenon and further developing this technology could help accelerate the transition to clean energy.

Abstract (150 words)

Several experiments have suggested that building a quantum engine using the electron spin enables the harvesting of thermal fluctuations on paramagnetic centers even though the device is at thermal equilibrium. We illustrate this thermodynamics conundrum through measurements on several devices of large output power, which endures beyond room temperature. We've inserted the Co paramagnetic center in Co phthalocyanine molecules between electron spin-selecting Fe/C₆₀ interfaces within vertical molecular nanojunctions. We observe output power as high as 450nW(24nW) at 40K(360K), which leapfrogs previous results, as well as classical spintronic energy harvesting strategies involving a thermal gradient. Our data links magnetic correlations between the fluctuating paramagnetic centers and output power. This device class also behaves as a spintronically controlled switch of current flow, and of its direction. We discuss the

conceptual challenges raised by these measurements. Better understanding the phenomenon and further developing this technology could help accelerate the transition to clean energy.

Main Text

Research on quantum thermodynamics has accelerated in recent years through model experiments on quantum heat and information engines^{1,2}. Testing electronics at this frontier of thermodynamics typically involves artificial quantum dots (QDs) with electronic states that require very low temperatures to be addressed discretely³⁻⁵. Here, the charge transport asymmetries between these states and the electrodes, which drive the heat engine's operation, are achieved by heterostructure design and electrostatic techniques. The engine's cycle typically requires feedback on the electronic occupation of one QD by another QD that is coupled to it. This generates heat or quantum information transfer between the QDs.

An elegant and industrially⁶ mature way of enhancing these transport asymmetries is to consider the electron spin. Spintronics research has generated several means⁷⁻¹⁰ of fully spin-polarizing a charge current. Several theoretical papers describe¹¹⁻¹³ a quantum spin-based engine that combines these so-called 'spintronic selectors' (SSs) with the discrete spin states of exchange-coupled paramagnetic (PM) centers. Following the second law of thermodynamics, such models relate the output of useful work to a temperature difference between the device's components.

Meanwhile, several groups have reported experimental spin engines¹⁴⁻¹⁶ operating at nominal thermal equilibrium. These experimental includes our recent report of 0.1nW at room temperature using the technologically relevant MgO magnetic tunnel junction¹⁶ (see Table 1). Here, contrary to most experimental quantum engine implementations³⁻⁵, the energy splitting between a PM center's spin states Δ is lower than the thermal energy $k_B T$ (see Fig. 1a). Thermal fluctuations on one PM center thus enable the stochastic population of both spin states on the PM center (circular arrows), and confer stochastic feedback on the spin occupation (vertical arrows) of the other PM center due to exchange coupling. Note how the spin engine's operation thus differs from the classical physics of spin caloritronics, which study how heat gradients can promote spin-based thermoelectric effects¹⁷.

A major conceptual challenge is thus to understand how, despite being at nominal thermal equilibrium¹⁴⁻¹⁶, it is possible for this device class to autonomously harvest thermal fluctuations on its PM centers as suggested^{15,16}. Furthermore, a major technical challenge is to aptly integrate PM centers and SSs so as to reproducibly achieve high output power at/beyond room temperatures. Indeed, control over discrete PM centers is routinely achieved only through single-spin experiments carried out using scanning tunnelling microscopes¹⁸⁻²⁰, but is only emerging for solid-state devices^{16,21,22}.

To circumvent the experimental difficulty¹⁶ of working with PM atoms, we used Co phthalocyanine (Pc) molecules, whose central Co atom exhibits a spin moment $S=1/2$ and forms an antiferromagnetic spin chain along molecular columns in thin²³ and ultrathin^{20,24} films. We inserted these molecules with a Co PM center into UHV-grown heterostructures that also comprise Fe/C₆₀ interfaces as spintronic selectors operating at/beyond room temperature⁹. The inferred^{25,26} spin-based potential profile across the nanojunction fulfills the spin engine's requirements^{15,16} (see Fig. 1b). Indeed, the highest occupied molecular orbital of CoPc, with strong Co *d* character, contains an unpaired electron spin²⁷ ($S=1/2$) on a z^2 orbital pointing out of the molecular plane. This orbital is nearly aligned with the Fe and Fe/C₆₀ Fermi levels E_F , thereby involving it in transport. The magnetic coupling^{24,28} between the ferromagnetic (FM) Fe and CoPc layers is weakened by inserting monolayers (ML) of C₆₀ molecules. The different C₆₀ spacer layer thicknesses (n and 5 ML) ensure that, due to spin-based asymmetries in transport fluctuations (arrow thicknesses in Fig. 1a) the lower SS dominates the spin-splitting of the $S=1/2$ state that occurs through spintronic anisotropy^{15,16,29,30}.

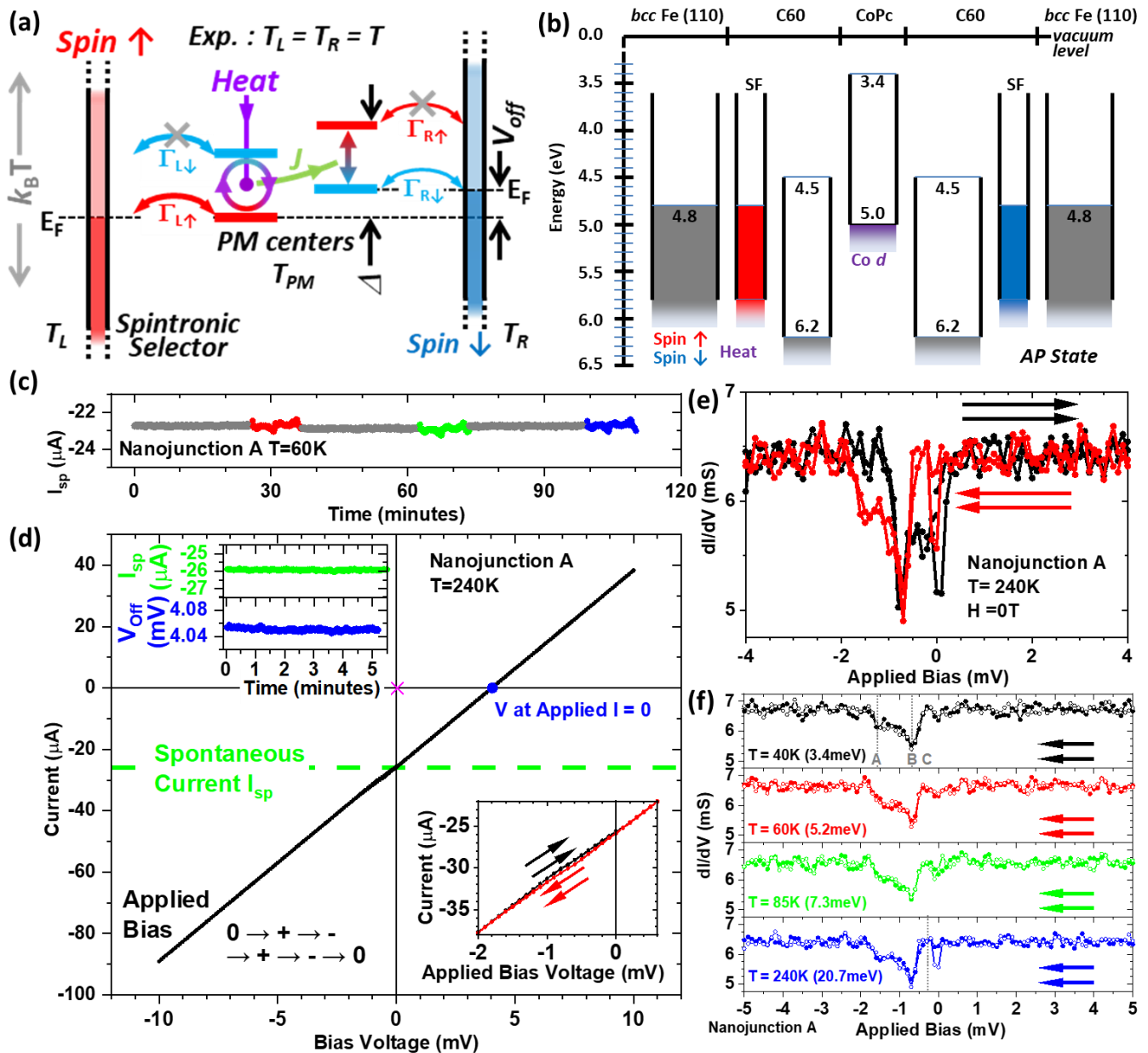


Figure 1: a molecule-based spin engine. (a) Schematic of the spin engine, in which thermal fluctuations on one PM center stochastically apply feedback to the spin population of a second PM center that is exchange-coupled to the first. Spin-conserved electron transfer to/from the PM center is rectified thanks to spintronic selectors. Implementation in a vertical molecular nanojunction: (b) energetical profile. The PM center is the Co site of CoPc molecules, while the spintronic selector is the Fe/C₆₀ interface. Data on metallic nanojunction A: (c) time dependence of I_{sp} and (d) $I(V)$ data at 240K. The magenta crosspoint is the experimental error. The top insets to panel (d) show the time dependence of I_{sp} and V_{off} , while the zoom around $V=0$ (lower inset) reveals an $I(V)$ hysteresis that contains features with a sub- $k_B T$ spectral resolution in (e) the current derivative dI/dV . Forward (black) and return (red) traces are shown. (f) Return dI/dV traces for 40K, 60K, 85K and 240K with essentially identical, sub- $k_B T$ spectral resolution.

We have crafted Fe/C₆₀/CoPc/C₆₀/Fe heterostructure into 300nm-diameter junctions thanks to a recently developed resist- and solvent-free nanojunction process²¹. Out of 193 junctions processed, 10 were neither open-circuit or short-

circuit, and 9 exhibited a combined current/voltage offset at least one order of magnitude larger than those observed on our measurement line using a calibrated resistance of similar amplitude. Other discarded possible artifacts are discussed hereafter in the Methods. We present data on 2 metallic (A, C) and 1 semiconducting (B) nanojunctions. The positive contact was connected to the junction's top electrode. All data were acquired with the sample at a constant, nominally uniform temperature T .

As illustrated using data acquired on metallic nanojunction A, these devices exhibit a large persistent non-zero spontaneous current $I_{sp} \sim -10\mu\text{A}$ (see Fig. 1c). Its amplitude is not strongly affected by intermittent sweeps of an external magnetic field up to 2T applied perpendicularly to the electrode magnetizations. This confirms that, in our implementation, the engine's primary energy source is not the external applied magnetic field^{11,14,31}. Rather, spintronic anisotropy between the spinterface and the PM centers generates an effective internal magnetic field that lifts the spin degeneracy on the PM center. We present in Fig. 1(d) repeated $I(V)$ sweeps at 240K. The slope resistance R_s calculated from current at $\pm 10\text{mV}$ is 157Ω . Comparing with the time dependence of I_{sp} plotted in the top inset, we find that the current remains constant whether $V=0$ is applied or not. This offset current $I_{off}=-26\mu\text{A}$, and the complementary bias offset $V_{off}=4.05\text{mV}$ (see the time dependence in the top inset), are respectively 230x and 100x larger than the experimental offset errors observed for a 100Ω calibrated resistance (magenta crosspoint in Fig. 1d).

The lower inset to Fig. 1(d) reveals a slight, hysteretic deviation from a linear response that depends on the sweep direction (red and black arrows). Within this 1.4mV bias window, the numerical derivative (see Fig. 1(e)) reveals features with a FWHM as low as 0.3meV despite an expected thermal smearing of $2-3k_B T$ upon transport, with $k_B T=20.7\text{meV}$ here. This sub- $k_B T$ spectral resolution is mostly unchanged upon reducing thermal fluctuations by a factor of 6, as are the main spectral features (denoted A, B and C in Fig. 1f).

These sub- $k_B T$ spectral features may be a signature of electronic noise reduction induced by a feedback mechanism³². They were also observed in our previous report¹⁶. Therein, we showed that the spin splitting on, and exchange coupling between, these energetically discrete states on the PM centers is driven by transport (more precisely spintronic anisotropy^{29,30}), and defines a complex bias-dependent transport landscape close to E_F ¹⁶. Once the applied bias causes these states to fall outside the dominant transport window, a linear $I(V)$ response ensues¹⁶. We therefore infer from the present 1.4meV window that, on a given state, the spin splitting Δ (see Fig. 1a) is at most 1.4meV, and is likely much lower given that several coupled PM states are involved. Since $T \geq 40\text{K}$ in our experiment, the spin engine's $k_B T > \Delta$ condition^{11,15,16} (see Fig. 1a) is always satisfied.

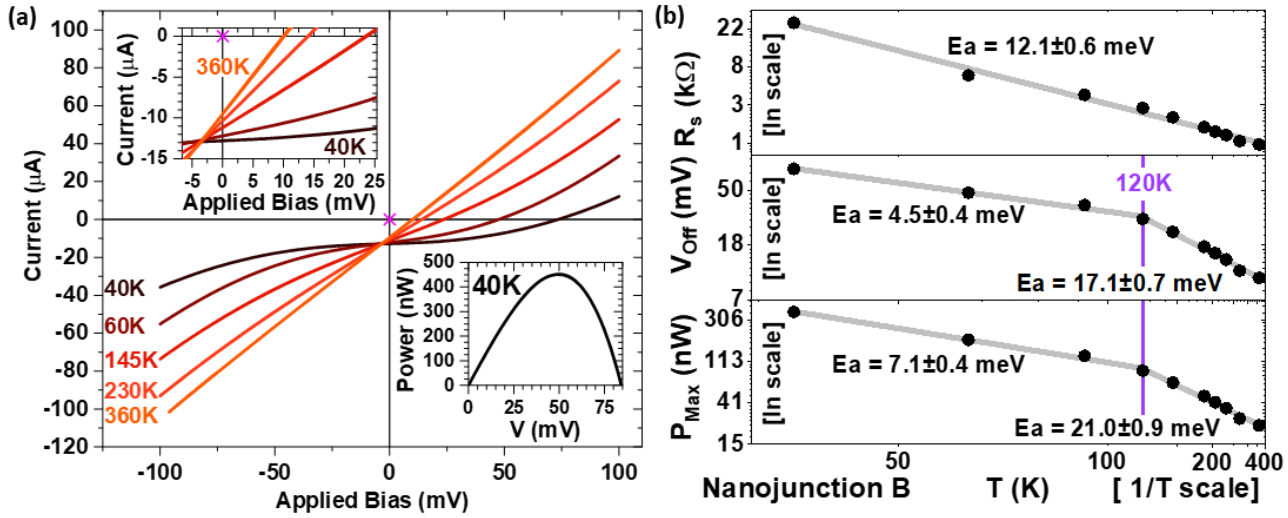


Figure 2: Thermally activated, large output electrical power across the nanoharvester. (a) $I(V)$ data from nanojunction B at $H=0T$ within $40 < T(K) < 360$. Top inset: zoom at low bias. Lower inset: $P(V)$ data showing $P_{Max} = 450\text{nW}$ at 40K. The magenta crosspoint is the experimental error. (b) \ln vs $1/T$ plots of (top) R_s , (middle) V_{Off} and (bottom) P_{Max} . P_{Max} decreases from 370nW at 40K to 24nW at 360K per two thermal activation regimes, with a 120K crossover temperature that may correspond to the exchange coupling between Co sites in CoPc molecular spin chains²³. The activation energy E_a is given for each regime.

The slight decrease in junction conductance with increasing temperature (see Fig. 1f) confirms the metallic nature of nanojunction A. This, and several other metallic nanojunctions, exhibit $17 < P_{Max}(\text{nW}) < 55$ for $150 < R_s(\Omega) < 800$ at 40K (not shown). Research on so-called tunnelling spintronic devices has shown that, due to discrete states within the barrier^{33–35}, spintronic regimes involving metallic and semiconducting nanochannels may coexist in a device³⁶. We now turn to semiconducting nanojunction B, for which we observe (see Fig. 2a) a mostly linear $I(V)$ at 360K ($R_s=1.05\text{k}\Omega$) that becomes increasingly non-linear as T is lowered to 40K ($R_s=25.9\text{k}\Omega$). Current and bias offsets that are orders of magnitude beyond experimental error^a for those R_s are observed at all temperatures, and reach (84mV, -13.8 μ A) at 40K (see lower inset of Fig. 2a).

As seen in the \ln vs. $1/T$ plots of Fig. 2(b), R_s decreases with increasing T following a thermal activation law of the form $R = R_0 e^{-\frac{E_a}{k_B T}}$ with a single activation energy E_a over $40 < T(K) < 360$. In contrast, V_{Off} and the maximum power P_{Max} both exhibit two activation regimes with a crossover at 120K. This thermal energy is qualitatively similar to the 70K exchange coupling energy between Co sites in CoPc molecular spin chains deposited onto Fe, which we observed through magnetotransport²¹. The difference in magnetic exchange energy could arise from a different templating effect^{23,37} induced here by the C_{60} underlayer.

These experimental data thus suggest that magnetic correlations between paramagnetic centers play a central role in the spin engine, as expected from theory^{11,13}. The lower thermally activated decrease in V_{Off} and P_{Max} for $40 < T(K) < 120$

^a Using calibrated resistances to determine experimental bias and current offsets, we obtain (1k Ω , 20 μ V, 30nA) and (10k Ω , 30 μ V, 0.8nA) (see magenta crosspoint in Fig. 2a and top inset). Also, this experimental offset explanation runs counter to I_{off} decreasing with decreasing R_s (see Fig. 2(a)). Once permanent electrostatic degradation causes R_s to decrease from 25.9k Ω to 8.1k Ω at 40K, we recover offsets within these boundaries.

arises from spin depolarization transport processes³⁸. The higher thermally activated decrease in V_{Off} and P_{Max} for $T > 120$ K reflects the additional loss of correlations in the paramagnetic fluctuations between the centers.

Spintronic selector	PM Center	T (K)	P_{Max} (nW)	Ref.
FM Metal	MnAs FM QDs in GaAs matrix	3	1	14
Spin filter tunnel barrier	Al QDs	1	10^{-5}	15
Co/C spinterface	C PM dimer in MgO	295	0.1	16
Fe/C ₆₀ spinterface	CoPc, between C ₆₀ layers	360	24	Present work.
		295	27	
		40	450	

Table 1: a comparison with reported spin engines. QD=quantum dot.

While the exact nanotransport path isn't known³⁹ here, we surmise that many of the nominal ≈ 98400 PM sites within the 3ML CoPc of our 300nm-diameter junctions are acting as thermal energy harvesters. This would explain $P_{Max} = 450$ nW at 40K (lower inset to Fig. 2(a)) — a 450x increase over the previous record measured at 3K and $H=1$ T¹⁴, and at 295K a 270x increase compared to our prior measurements¹⁶ on the single C dimer of PM centers within a MgO junction. At 360K, $P_{Max}=24$ nW. Table 1 compares our results with previous experiments^{14–16} on spin engines.

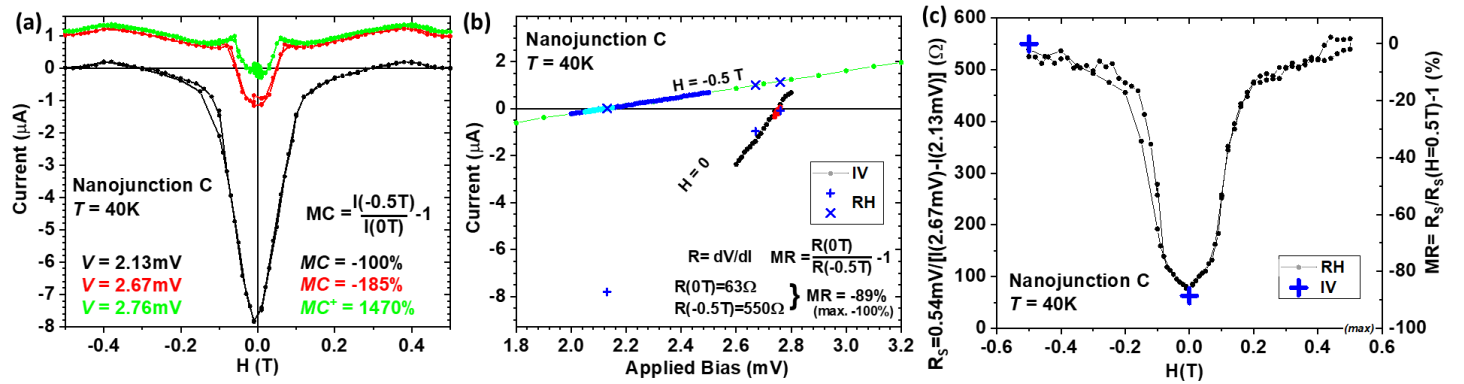


Figure 3: Spintronic features of the thermal energy harvester. (a) $I(H)$ data acquired on nanojunction C at 40K. (b) $I(V)$ data at $H=0$ T and $H=-0.5$ T, revealing a linear behavior with $R_S=63\Omega$ and $R_S=550\Omega$ around $V_{Off}=2.13$ mV and $V_{Off}=2.76$ mV, respectively. The blue crosses reflect the $I(H)$ data from panel a. (c) $R_S(H)$ calculated from two $I(H)$ datasets from panel (a). The blue crosses indicate R_S inferred from panel b. The two spintronic V_{Off} lead to extremal values of $-100 < MC$ (%) $< \infty$ in $I(H)$ data, as do the two spintronic R_S regarding $-100 < MR$ (%) $< \infty$.

To illustrate the spintronic nature of this thermal energy harvesting, and features of this device class, we present in Fig. 3 data acquired on metallic nanojunction C at 40K with H applied mostly in-plane. $I(H)$ data reveal a strong H dependence of junction current, which saturates for $|H| > 0.5$ T (not shown). We deduce that the parallel orientation of FM electrode magnetization is reached at $|H|=0.5$ T. The current can be suppressed at $H=0$ and $H=-0.5$ T for $V_{Off}=2.76$ mV and $V_{Off}=2.13$ mV, respectively. Thus, the junction's two magnetic states promote differing V_{Off} . They also drive a sign change in current at $V=2.67$ mV, with $I=\pm 1\mu$ A. These (V, I) pairs are orders of magnitude beyond experimental offset errors determined using a calibrated resistance.

These V_{Off} are corroborated through multiple $I(V)$ data (Fig. 3b). The H dependence of R_S , calculated using $I(H)$ data from panel a, is shown in Fig. 3c. Consistency between these three data panels is visualized by blue crosses in panels b and c.

The magnetoresistance $MR = \frac{R_S(0T)}{R_S(-0.5T)} - 1$, with a $-100 < MR(\%) < \infty$ range, reaches -89%. As a rough estimate using

the Julliere model⁴⁰, the corresponding 'optimistic' $MR' = \frac{R_S(-0.5T)}{R_S(0T)} - 1 = 770\%$ implies an average transport spin polarization $P = 89.1\%$ of the two Fe/C₆₀ spintronic selectors⁹. The magnetocurrent MC is $MC = \frac{I(-0.5T)}{I(0T)} - 1$. The $MC = -100\%$ and $MC = 1470\%$ measured at each V_{off} constitute experimental verification of the expected $-100 < MC(\%) < \infty$ range when the currents in each magnetic state are of same sign. Finally, at $V = 2.67\text{mV}$, $MC = -185\%$ (see panel a) because of opposite signs of the current. This device class thus behaves as a spintronically controlled switch of current flow, and of its direction.

As in previous spin engines experiments¹⁴⁻¹⁶, our nanodevices generate electrical power even though all device components (electrodes and PM centers) are nominally at the same temperature. Numerous possible artifacts have been considered and discarded (see main text, footnote a) and Methods). However, a current flowing between non-magnetic leads across a PM center can locally raise its temperature^{41,42}, by lifting its spin degeneracy and by altering the exchange coupling between a pair of PM center^{30,43}. Current-induced entropy production on the PM centers is possible even without a temperature difference between the leads⁴⁴. Furthermore, non-linear transport can promote local deviations from thermal equilibrium, e.g. quantum magnetic fluctuations due to spin-shot noise^{45,46}. This suggests different temperatures in the spin engine for the conduction electrons, for the FM magnetization and the FM's atomic lattice⁴⁷.

Miao et al. report¹⁵ that power output does not require that current initially flow across the device. We suggest that the thermodynamical imbalance may also be due to thermodynamical induction^{48,49}, which is possible in our hopping transport regime. Here, at constant T, fast spin dynamics on the PM center can generate slow changes to the charge current and FM electrode magnetization.

To explain spontaneous currents for minutes/hours (see Fig. 1c), Joule heating within metallic pinholes in the junction must be discarded. Instead, 'quantum friction', *i.e.* quantum fluctuations between eigenstates leading to decoherence, may be low. Indeed, spin excitations on the CoPc PM center are long-lived due to weak spin-lattice and spin-orbit interactions⁵⁰⁻⁵², while any spin relaxation to the electrodes⁵⁰⁻⁵² is attenuated due to their high transport spin polarization (see Fig. 3c and Ref. 16). Future thermodynamical modelling^{11-13,16,47} of the spin engine should account for the entropy decrease induced by the FM state of the electrodes⁵³, and consider the long-lived⁵⁴ dynamics of magnetic coupling between the FM electrode and PM center induced by spintronic anisotropy.

To conclude, we have observed very large electrical power generation beyond room temperature, which we link to the magnetic correlations between fluctuating paramagnetic centers placed within a spin-based quantum engine. We hope that these results and discussion shall stimulate very fertile research to better understand this phenomenon at the intersection between spintronics and quantum thermodynamics. One may increase power output by tuning each ingredient of the spin engine, from the magnetic coupling between PM centers to the spintronic anisotropy exerted on these centers by the spintronic selectors. The most promising path to market is a MgO implementation¹⁶, which benefits from industrially large device areal densities in industrial products. Harvesting this most basic form of energy --- ambient thermal energy, could help to alter our nomadic needs for energy storage and accelerate the transition to clean energy.

Methods

Si/SiO_x/Cr(5)/Fe(50)/C₆₀(*n* ML)/CoPc(3ML)/C₆₀(5ML)/Fe(10)/Cr(50) heterostructure stacks were grown in-situ and at room temperature in an ultra-high vacuum multichamber cluster by dc sputtering (metals) and thermal evaporation (CoPc). All numbers are in nm; 1ML C₆₀=0.9nm. 1ML CoPc=0.4nm. The SiO_x substrate was annealed at 110°C and allowed to cool down prior to deposition. The C₆₀ thickness *n* for nanojunctions A, B and C was 3ML, 1ML and 1ML, respectively. Nanojunctions were crafted²¹ using 300nm-diameter SiO₂ nanobeads and were wirebonded to a sample chip.

Measurements tool place the dark using an electrically grounded cryostat and long metallic wires⁵⁵. An external microwave excitation is thus unrealistic. The change in sign of the current with H (see Fig. 3a) and the voltage amplitude (up to 74mV, see Fig. 2b) both point against a thermovoltage drop along the leads. The effect persists at T=40K when the sample heater is turned off, and decreases with increasing temperature. This casts aside a black-body radiation effect, as well as any stray T gradient between the cryostat's cold finger and the sample. Reference nanojunctions²¹ containing only a CoPc spacer layer yielded current- and bias-offsets within the range found using calibrated resistances.

Acknowledgements

We thank J. Arakshi for invaluable support with sample growth, P. Potts, R. Sanchez, R. Whitney and Y. Henry for stimulating discussions, B. Doudin for collaborating on nanobead processing, the remaining members of the STNano technological platform staff for technical assistance with certain processing steps, and the IPCMS machine shop for support⁵⁵. Work was performed using Synchrotron SOLEIL beamtime proposals 20170317 and 20180169. We acknowledge financial support from from the Region Grand Est and Synchrotron SOLEIL, from CEFIPRA grant 5604-3, from the ANR (ANR-06-NANO-033-01, ANR-09-JCJC-0137, ANR-14-CE26-0009-01), the Labex NIE "Symmix" (ANR-11-LABX-0058 NIE), the EC Sixth Framework Program (NMP3-CT-2006-033370), the Contrat de Plan Etat-Region grants in 2006 and 2008, by « NanoTérahertz », a project co-funded by the ERDF 2014-2020 in Alsace (European Union fund) and by the Region Grand Est through its FRCR call, by the impact project LUE-N4S part of the French PIA project "Lorraine Université d'Excellence", reference ANR-15IDEX-04-LUE and by the « FEDER-FSE Lorraine et Massif Vosges 2014-2020 », a European Union Program.

Authors Contributions

M.B conceived the experiment. B.C., C.K. and V.d.C. grew the samples. L.K. made the nanojunctions, with help from D.M., A.B., R.B. and B.C. . B.C., M.B. and L.K. performed measurements with help from L. J., E.M., S.M., E.S, F.C. and P.O. . M.B., B.C. and L.K. analyzed the data, with input from M.H., F.M., B.V., D.L., W.W. and S.B. . M.B. wrote the manuscript, with input from all authors.

References

1. Strasberg, P., Schaller, G., Brandes, T. & Esposito, M. Quantum and Information Thermodynamics: A Unifying Framework Based on Repeated Interactions. *Physical Review X* **7**, 021003 (2017).
2. Benenti, G., Casati, G., Saito, K. & Whitney, R. S. Fundamental aspects of steady-state conversion of heat to work at the nanoscale. *Physics Reports* **694**, 1–124 (2017).
3. Thierschmann, H. *et al.* Three-terminal energy harvester with coupled quantum dots. *Nature Nanotechnology* **10**, 854–858 (2015).
4. Josefsson, M. *et al.* A quantum-dot heat engine operating close to the thermodynamic efficiency limits. *Nature Nanotechnology* **13**, 920–924 (2018).
5. Koski, J. V., Kutvonen, A., Khaymovich, I. M., Ala-Nissila, T. & Pekola, J. P. On-Chip Maxwell's Demon as an Information-Powered Refrigerator. *Physical Review Letters* **115**, 260602 (2015).

6. Kent, A. D. & Worledge, D. C. A new spin on magnetic memories. *Nat Nano* **10**, 187–191 (2015).
7. Bowen, M. *et al.* Half-metallicity proven using fully spin-polarized tunnelling. *Journal of Physics: Condensed Matter* **17**, L407–L409 (2005).
8. Ikeda, S. *et al.* Tunnel magnetoresistance of 604% at 300K by suppression of Ta diffusion in CoFeB/MgO/CoFeB pseudo-spin-valves annealed at high temperature. *Applied Physics Letters* **93**, 082508 (2008).
9. Djeghloul, F. *et al.* High Spin Polarization at Ferromagnetic Metal-Organic Interfaces: a Generic Property. *J. Phys. Chem. Lett.* **7**, 2310–2315 (2016).
10. Liu, H. *et al.* Giant tunneling magnetoresistance in epitaxial Co₂MnSi/MgO/Co₂MnSi magnetic tunnel junctions by half-metallicity of Co₂MnSi and coherent tunneling. *Applied Physics Letters* **101**, 132418 (2012).
11. Ptaszyński, K. Autonomous quantum Maxwell's demon based on two exchange-coupled quantum dots. *Physical Review E* **97**, 012116 (2018).
12. Tang, G., Thingna, J. & Wang, J. Thermodynamics of energy, charge, and spin currents in a thermoelectric quantum-dot spin valve. *Physical Review B* **97**, 155430 (2018).
13. Ptaszyński, K. & Esposito, M. Thermodynamics of Quantum Information Flows. *Physical Review Letters* **122**, 150603 (2019).
14. Hai, P. N., Ohya, S., Tanaka, M., Barnes, S. E. & Maekawa, S. Electromotive force and huge magnetoresistance in magnetic tunnel junctions. *Nature* **458**, 489–492 (2009).
15. Miao, G.-X., Chang, J., Assaf, B. A., Heiman, D. & Moodera, J. S. Spin regulation in composite spin-filter barrier devices. *Nature Communications* **5**, 3682–3687 (2014).
16. Katcko, K. *et al.* Spin-driven electrical power generation at room temperature. *Communications Physics* **2**, 116 (2019).
17. Tu, S. *et al.* Record thermopower found in an IrMn-based spintronic stack. *Nat Commun* **11**, 1–7 (2020).
18. Verlhac, B. *et al.* Atomic-scale spin sensing with a single molecule at the apex of a scanning tunneling microscope. *Science* **366**, 623–627 (2019).
19. Natterer, F. D. *et al.* Reading and writing single-atom magnets. *Nature* **543**, 226–228 (2017).

20. Chen, X. *et al.* Probing Superexchange Interaction in Molecular Magnets by Spin-Flip Spectroscopy and Microscopy. *Physical Review Letters* **101**, 197208 (2008).
21. Katcko, K. & *et al.* Encoding information on the excited state of a molecular spin chain. *submitted*.
22. Barraud, C. *et al.* Unidirectional Spin-Dependent Molecule-Ferromagnet Hybridized States Anisotropy in Cobalt Phthalocyanine Based Magnetic Tunnel Junctions. *Phys. Rev. Lett.* **114**, 206603 (2015).
23. Serri, M. *et al.* High-temperature antiferromagnetism in molecular semiconductor thin films and nanostructures. *Nat Commun* **5**, 3079–3087 (2014).
24. Gruber, M. *et al.* Exchange bias and room-temperature magnetic order in molecular layers. *Nat Mater.* **14**, 981–984 (2015).
25. Ma, Z., Zhao, J., Wang, X. & Yu, J. Effect of bulk and planar heterojunctions based charge generation layers on the performance of tandem organic light-emitting diodes. *Organic Electronics* **30**, 136–142 (2016).
26. Błoński, P. & Kiejna, A. Calculation of surface properties of bcc iron. *Vacuum* **74**, 179–183 (2004).
27. Bartolomé, J., Monton, C. & Schuller, I. K. Magnetism of Metal Phthalocyanines. in *Molecular Magnets* (eds. Bartolomé, J., Luis, F. & Fernández, J. F.) 221–245 (Springer Berlin Heidelberg, 2014). doi:10.1007/978-3-642-40609-6_9.
28. Boukari, S. *et al.* Disentangling Magnetic Hardening and Molecular Spin Chain Contributions to Exchange Bias in Ferromagnet/Molecule Bilayers. *Nano Letters* **18**, 4659 (2018).
29. Misiorny, M., Hell, M. & Wegewijs, M. R. Spintronic magnetic anisotropy. *Nat Phys* **9**, 801–805 (2013).
30. Fransson, J., Ren, J. & Zhu, J.-X. Electrical and Thermal Control of Magnetic Exchange Interactions. *Physical Review Letters* **113**, 257201 (2014).
31. Ralph, D. C. The electromotive force of MnAs nanoparticles. *Nature* **474**, E6 (2011).
32. Wagner, T. *et al.* Strong suppression of shot noise in a feedback-controlled single-electron transistor. *Nature Nanotechnology* **12**, 218–222 (2017).
33. Schleicher, F. *et al.* Localized states in advanced dielectrics from the vantage of spin- and symmetry-polarized tunnelling across MgO. *Nature Communications* **5**, 4547 (2014).

34. Taudul, B. *et al.* Tunneling Spintronics across MgO Driven by Double Oxygen Vacancies. *Advanced Electronic Materials* 1600390 (2017) doi:10.1002/aelm.201600390.
35. Schleicher, F. *et al.* Consolidated picture of tunnelling spintronics across oxygen vacancy states in MgO. *J. Phys. D: Appl. Phys.* **52**, 305302 (2019).
36. Teixeira, J. M. *et al.* Tunneling processes in thin MgO magnetic junctions. *Applied Physics Letters* **96**, 262506 (2010).
37. Heutz, S. *et al.* Molecular Thin Films: A New Type of Magnetic Switch. *Advanced Materials* **19**, 3618–3622 (2007).
38. Miao, G.-X., Münzenberg, M. & Moodera, J. S. Tunneling path toward spintronics. *Rep. Prog. Phys.* **74**, 036501–036519 (2011).
39. Studniarek, M. *et al.* Probing a Device's Active Atoms. *Advanced Materials* 1606578 (2017) doi:10.1002/adma.201606578.
40. Julliere, M. Tunneling between ferromagnetic films. *Physics Letters A* **54**, 225–226 (1975).
41. Núñez, A. S. & Duine, R. A. Effective temperature and Gilbert damping of a current-driven localized spin. *Phys. Rev. B* **77**, 054401 (2008).
42. Díaz, S. & Núñez, Á. S. Current-induced exchange interactions and effective temperature in localized moment systems. *Journal of Physics: Condensed Matter* **24**, 116001 (2012).
43. Saygun, T., Bylin, J., Hammar, H. & Fransson, J. Voltage-Induced Switching Dynamics of a Coupled Spin Pair in a Molecular Junction. *Nano Lett.* **16**, 2824–2829 (2016).
44. Jaramillo, J. D. V. & Fransson, J. Charge Transport and Entropy Production Rate in Magnetically Active Molecular Dimer. *J. Phys. Chem. C* **121**, 27357–27368 (2017).
45. Qaiumzadeh, A. & Brataas, A. Quantum magnetization fluctuations via spin shot noise. *Physical Review B* **98**, (2018).
46. Zholud, A., Freeman, R., Cao, R., Srivastava, A. & Urazhdin, S. Spin Transfer due to Quantum Magnetization Fluctuations. *Physical Review Letters* **119**, (2017).
47. Wegrowe, J.-E., Ciornei, M. C. & Drouhin, H.-J. Spin transfer in an open ferromagnetic layer: from negative damping to effective temperature. *Journal of Physics: Condensed Matter* **19**, 165213 (2007).

48. Patitsas, S. N. Cooling by Thermodynamic Induction. *Journal of Low Temperature Physics* **186**, 316–346 (2017).
49. Patitsas, S. N. Thermodynamic induction effects exhibited in nonequilibrium systems with variable kinetic coefficients. *Phys. Rev. E* **89**, 012108 (2014).
50. Warner, M. *et al.* Potential for spin-based information processing in a thin-film molecular semiconductor. *Nature* **503**, 504–508 (2013).
51. Bader, K., Winkler, M. & van Slageren, J. Tuning of molecular qubits: very long coherence and spin–lattice relaxation times. *Chemical Communications* **52**, 3623–3626 (2016).
52. Atzori, M. & Sessoli, R. The Second Quantum Revolution: Role and Challenges of Molecular Chemistry. *J. Am. Chem. Soc.* **141**, 11339–11352 (2019).
53. Bormashenko, E. Entropy, Information, and Symmetry; Ordered Is Symmetrical, II: System of Spins in the Magnetic Field. *Entropy* **22**, 235 (2020).
54. van Hoogdalem, K. A., Albert, M., Simon, P. & Loss, D. Proposal for a Quantum Magnetic R C Circuit. *Physical Review Letters* **113**, (2014).
55. Joly, L. *et al.* Versatile variable temperature insert at the DEIMOS beamline for *in situ* electrical transport measurements. *Journal of Synchrotron Radiation* **23**, 652–657 (2016).